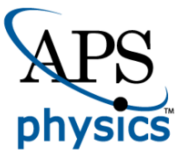

Wing-pitch modulation in maneuvering fruit flies is explained by an interplay between aerodynamics and a torsional spring

Tsevi Beatus and Itai Cohen

Phys. Rev. E **92**, 022712 — Published 14 August 2015

DOI: 10.1103/PhysRevE.92.022712

Wing-pitch modulation in maneuvering fruit flies is explained by an interplay between aerodynamics and a torsional spring

Tsevi Beatus and Itai Cohen
Department of Physics, Cornell University, Ithaca, New York 14853, USA

While the wing kinematics of many flapping insects have been well characterized, understanding the underlying sensory, neural, and physiological mechanisms that determine these kinematics is still a challenge. Two main difficulties in understanding the physiological mechanisms arise from the complexity of the interaction between a flapping wing and its own unsteady flow, as well as the intricate mechanics the insect wing-hinge, which is among the most complicated joints in the animal kingdom. These difficulties call for the application of reduced-order approaches. Here, this strategy is used to model the torques exerted by the wing-hinge along the wing-pitch axis of maneuvering fruit flies as a damped torsional spring with elastic and damping coefficients as well as a rest angle. Furthermore, we model the air flows using simplified quasi-static aerodynamics. Our findings suggest that flies take advantage of the passive coupling between aerodynamics and the damped torsional spring to indirectly control their wing-pitch kinematics by modulating the spring parameters. The damped torsional-spring model explains the changes measured in wing-pitch kinematics during roll correction maneuvers through modulation of the spring damping and elastic coefficients. These results, in conjunction with the previous literature, indicate flies can accurately control their wing-pitch kinematics on a sub-wing-beat time-scale by modulating all three effective spring parameters on longer time-scales.

I. INTRODUCTION

Insects were the first animals on Earth to evolve flight about 350 million years ago and can perform a wide array of extreme aerial maneuvers with exquisite accuracy and robustness [1, 2]. The mechanisms of insect flight are multi-layered, spanning a wide range of length and time scales: genetics and cellular mechanisms, sensory mechanisms, neural networks, muscular morphology and actuation, wing kinematics and aerodynamics, all combine to elicit a complex and graceful animal behavior. Developing an understanding of flapping flight at each of these layers presents unique challenges. At the neuro-muscular level for example, efforts are being made to determine how neural circuits are configured to provide precise activation of wing muscles with fast feedback at the single wing-stroke timescale [3–10].

The level of flight mechanics, which is the focus of this work, requires developing an understanding of how the wing kinematics and aerodynamic mechanisms enable insects to generate the forces and torques required to fly, maneuver, and mitigate the aerodynamic instabilities inherent to their flapping [11–22]. However, understanding the underlying mechanisms that generate these wing kinematics remains a challenge for two main reasons. First, the interaction of the wing with its own unsteady flow field is highly complex [12, 15, 16, 23–28], similarly to other fluid-structure problems [29–32]. Second, the wing-hinge of insects is among the most complicated joints in the animal kingdom [33, 34]. In flies, for example, it consists of multiple steering muscles, tendons and both flexible and rigid parts. These elements intertwine into a transmission mechanism that both redirects power from the main flight muscles to the wing and allows fine-tuned control over the wing motion [5, 7, 34–36]. Although the morphology of the wing hinge is known and the neural activation patterns of several steering muscles have been measured [4–7], the dynamics of the wing hinge is still unclear, both due to its mechanical complexity as well as the intricate neural activity of each of its muscles. Only recently it has become possible to visualize muscles of the wing hinge in action [37].

Remarkably, this seemingly intractable behavior can often be summarized by a reduced-order approach in which the wing-hinge and the fluid-structure interactions are represented by simplified models. This strategy has been used very successfully to estimate the aerodynamic forces arising from complex flows using quasi-static models [12, 14, 38] and describe some basic aspects of animal locomotion control with linear control theory [19–22, 39–48]. This reduced order approach is useful because it provides a framework for characterizing the complex behaviors and a well defined functional target that can guide the process of determining the underlying mechanism generating the behavior.

Here, we take such an approach in explaining the kinematics of the wing-pitch angle of maneuvering fruit flies. This degree-of-freedom describes the rotation of a wing about its leading edge. Hence, the wing-pitch angle directly determines the wing's angle-of-attack, which is, together with the wing speed, a key parameter governing the magnitude and direction of the aerodynamic force generated by the wing [14].

Several pioneering studies have suggested that wing-pitch kinematics are passively determined by a balance between aerodynamic and elastic torques, as well as the inertia of the moving wing [49–56]. Subsequently, a number of studies have used torsional-spring models to describe wing-pitch kinematics in mechanical [57–64] and computational [63, 65–72] models of flapping wings, as well as to describe wing-pitch kinematics of free-flying fruit flies [73]. For example, the latter study showed that

the torques produced by the wing hinge to control wing-pitch can be effectively modeled as those arising from a damped torsional spring. Furthermore, the study showed that simple modification of the spring rest angle generates wing-pitch asymmetries that result in body yaw turns.

Here, we measure the body and wing kinematics of fruit files during roll correction maneuvers and model their wing-hinge as a torsional spring with three parameters: elastic coefficient, damping coefficient, and pitch rest-angle. We find that the fly's wing-pitch kinematics are accurately explained by an interplay between the spring torque and aerodynamic torque. Moreover, the torsional-spring model explains the measured, sub-wing-beat modulation of the wing-pitch angle during roll maneuvers as resulting from an increase in both the spring damping and elastic coefficient that occurs on a slower, single wing-beat timescale. Thus, in addition to modulation of the rest angle reported in prior work, we find that flies can modulate all three spring parameters to control wing pitch. These results also give rise to a number of open questions regarding the physiological origin of the three spring parameters, their mode of actuation, and their dependence on the wing stroke angle.

II. EXPERIMENTAL METHODS

We mechanically perturbed fruit flies (*Drosophila melanogaster*) in mid-air, filmed their correction maneuvers using high-speed video, and measured their body and wing kinematics. To exert mid-air roll perturbations we glued a $1.5-2$mm long magnetic carbon-steel pin to the back of each fly, on the dorsal surface of its thorax, and applied short magnetic field pulses that rolled the flies (Fig. 1a). The pin did not interfere with the motion of the wings and added 20% to the fly's mass, which did not alter its flight as compared with control experiments with untreated flies. The change in the body center of mass position due to the pin was small, about 3.5% of the body length. Further experimental details, including the small effect of the pin on the body inertia tensor, are discussed in [21]. In each experiment $\sim$15 prepared flies were released in a transparent cubic chamber of side length 13cm, equipped with two Helmholtz coils that are used to generate a vertical magnetic field [19, 21]. Three synchronized fast cameras (Phantom v7.1, Vision Research) were focused on a cubic sub-volume at the center of the chamber. The cameras were orthogonal to each other and operated at 8000 frames^{-1} and 512×512 pixel resolution.

Recording was initiated by an optical trigger detecting when a fly enters the filming volume and triggering the cameras as well as a 5ms (1 wing-beat) vertical magnetic pulse generated by the two Helmholtz coils. Controlling the voltage across the coils enables us to vary the magnetic field strength up to $\sim10^{-2}$Tesla, which is about 1000 times stronger than the Earth's magnetic

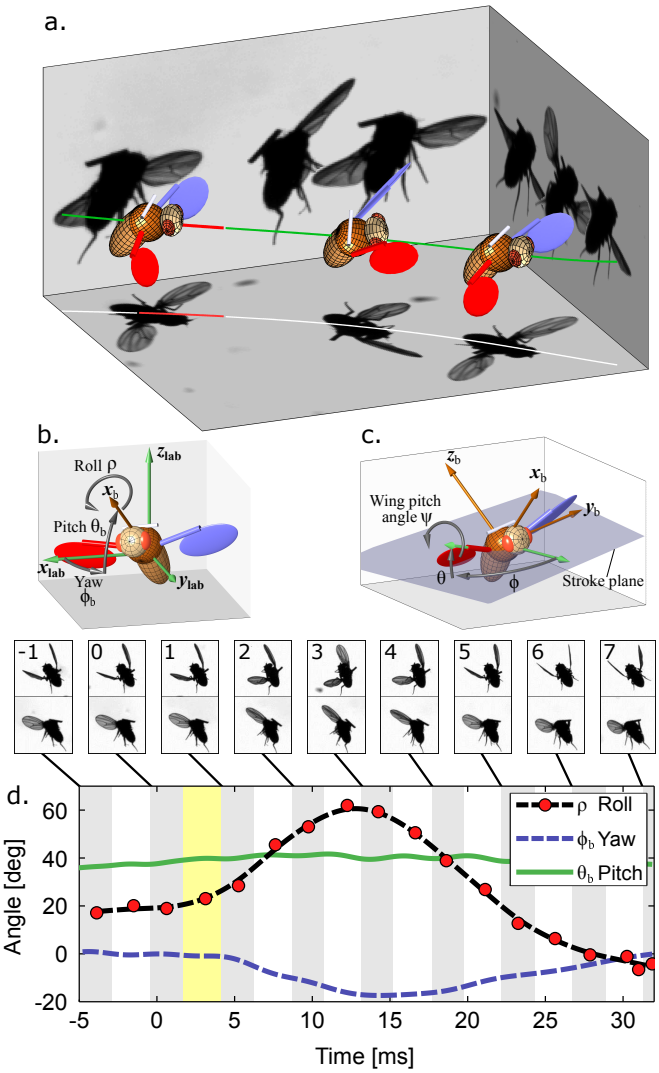

FIG. 1. (Color online) Roll correction maneuver following a mid-air impulsive perturbation. (a) Superimposed images from 3 orthogonal cameras of the fly during the maneuver. The 3D-rendered fly represents the measured kinematics. The perturbation location (red (dark gray) line) is shown on the fly's center-of-mass trajectory in green (light gray). In the second snapshot the fly is deflected 45° to its right with respect to its pre-perturbation roll angle. (b) Definition of body Euler angles with respect to the lab frame. $\hat{\mathbf{x}}_\mathrm{b}$ is the long body axis. (c) Definition of the body frame $(\hat{\mathbf{x}}_\mathrm{b}, \hat{\mathbf{y}}_\mathrm{b}, \hat{\mathbf{z}}_\mathrm{b})$ and wing Euler angles, measured in the body frame with respect to the stroke plane shown in shaded blue (dark gray). The wing pitch angle ψ describes the rotation of the wing about its vein, or leading edge, vector is shown for the right wing by a curved arrow. A pitch angle of ψ=0° implies that the wing is parallel to the wing stroke plane with the leading edge ahead of the wing surface. (d) Body Euler angles versus time. Perturbation was applied between $0-5$ms in yellow (black vertical lines). White and gray stripes represent forward and back strokes, respectively. Roll was measured manually at the middle of each half-stroke and smoothed by a spline (dashed black line). Measurement errors are smaller than the symbols size. The snapshots above the plot show top side-views of 9 consecutive wing-strokes of the maneuver, taken when the wings are at their forward-most position. The perturbation wing-beat is numbered 0.

field. Since fruit flies fly with their body axis pitched up at ∼45° and since the moment of inertia along their body axis is smaller than along the other axes, the largest deflection is generated along the body roll axis, with smaller perturbations along pitch and yaw (Fig. 1) [21].

We analyzed 10 flight sequences from 9 individual flies that were subject to roll perturbations of 35−70°. This range of perturbation angles was achieved by setting the amplitude of the current pulse through the Helmholtz coils during each experiment, such that increasing the current resulted in larger perturbation torque. In each maneuver, the fly performed a steady flight before and after the correction maneuver. Using a custom image analysis algorithm, we extracted a 3D kinematic description of the fly (Fig. 1a) consisting of its body position and orientation (defined in Fig. 1b) as well as the Euler angles – wing-stroke angle ϕ, wing elevation angle θ and wing-pitch angle ψ – for both wings (defined in Fig. 1c). Importantly, the wing Euler angles are define with respect to the stroke place in the body frame of reference, which is the relevant frame of reference for discussing wing actuation. While in some insects, such as locusts, wing deformation is considerable and induces significant aerodynamic effects [74], in *D. melanogaster* wing flexibility is small and the aerodynamic forces are well described by a flat rigid wing [14, 55]. Our measurements of *D. melanogaster* indicate that wing bending is negligible during most of the wing stroke and reaches no more than 5° during the wing's rapid (< 0.3ms) rotation between the down-stroke and up-stroke. Hence, in analyzing the wing kinematics we assume a flat rigid wing defined by its vein and chord vectors. Our motion tracking algorithm is based on using the movies from the three cameras to reconstruct a 3D hull of the fly for each frame, segmenting the hull into a body and two wings, and extracting the position and orientation of each part. The algorithm is described in detail in [21, 75].

III. RESULTS

A. Wing-pitch angle is modulated during roll maneuvers

Recently it has been shown that the main mechanism flies use to correct for roll perturbations is an asymmetric change of the stroke amplitude between both wings [21]. Here, we show that in addition to actuating the stroke angles, flies also modulate their wing-pitch angles and that these two degrees of freedom are strongly coupled. Hence, before discussing the role of wing-pitch and the way it is modulated, we will briefly review the kinematics of the wing-stroke angle during roll correction maneuvers.

A typical roll correction maneuver, in which a fly recovered from a 45° right roll perturbation, is shown in Fig. 1a. The body Euler angles, roll (ρ), yaw ($\phi_{\rm b}$), and pitch ($\theta_{\rm b}$), are plotted in Fig. 1d. Prior to the perturbation the fly was flying forward and slightly sideways with a stable roll angle of 20°. Following the 5ms magnetic torque (yellow strip) the roll angle increased to a maximum of 65° at t=13ms after the onset of the perturbation. The fly actively corrected and by t=30ms rolled back to ρ=0°, maintaining forward flight.

To correct for the perturbation the fly flapped asymmetrically for 3−4 wing-beats such that the right wing increased its stroke amplitude and the left wing decreased its stroke amplitude (the wing stroke angle ϕ is defined in Fig 1c). As soon as 3ms after the onset of the perturbation an amplitude asymmetry of 3° was observed and by 5ms the asymmetry increased to 11°. The asymmetry is evident in the top-view snapshots above Fig. 1d, taken each time the wings reach their forward-most position along the stroke. The wing stroke angles and their amplitude for both wings are plotted as a function of time in Fig. 2a,b. The extrema of the stroke amplitudes were observed around t=13ms, when the right wing amplitude (red) increased by 27° at its peak and the left wing amplitude (blue) decreased by 18° at its minimum. The stoke amplitude asymmetry is the main mechanism flies use to generate roll corrective torque and it is well described by the output of a proportional-integral (PI) controller model, as has been recently reported in [21]. After t=23ms the stroke amplitude asymmetry was reversed and the left wing stroke amplitude was larger than the right stroke amplitude, corresponding to a roll counter-torque that brakes the body roll velocity, allowing for faster corrective torque and, hence, faster correction time. Similar counter torques are typical also in body-pitch correction maneuvers following impulsive perturbations [22].

The measured wing kinematics show that in addition to the wing-stroke angle, the wing-pitch and elevation angles undergo substantial changes as well (Figs. 2c,d). Here, we take advantage of previously developed reduced order models for the pitch torques to determine how insects are changing the wing pitch angles ψ during a roll correction maneuver. This angle describes the rotation of each wing about its leading edge, or wing vein (Fig. 2c) and determines the wing angle of attack, a crucial aerodynamic parameter for generating aerodynamic forces.

We define ψ=0° when the wing surface is parallel to the stroke plane with the leading edge closer to the fly's head. The direction in which ψ increases is indicated by a curved arrow in Fig. 1c, such that a wing with ψ=90° is vertical to the stroke plane with the leading edge above the wing surface. To highlight changes in the spatial dependence of ψ during each stroke of the maneuver, we make a Lissajous-Bowditch plot of ψ as a function of the wing-stroke angle, ϕ, for each wing-beat separately (Fig. 2e). Each of the six plots in Fig. 2e shows a cycle in the (ϕ, ψ) plane corresponding to a single wing-beat during the maneuver. Each wing-beat starts when the wings are at their backward-most position, corresponding to a local maximum of ϕ (marked by black squares), and the motion in the (ϕ, ψ) plane is clockwise. The inset on each plot is a top view snapshot of the fly taken when ϕ

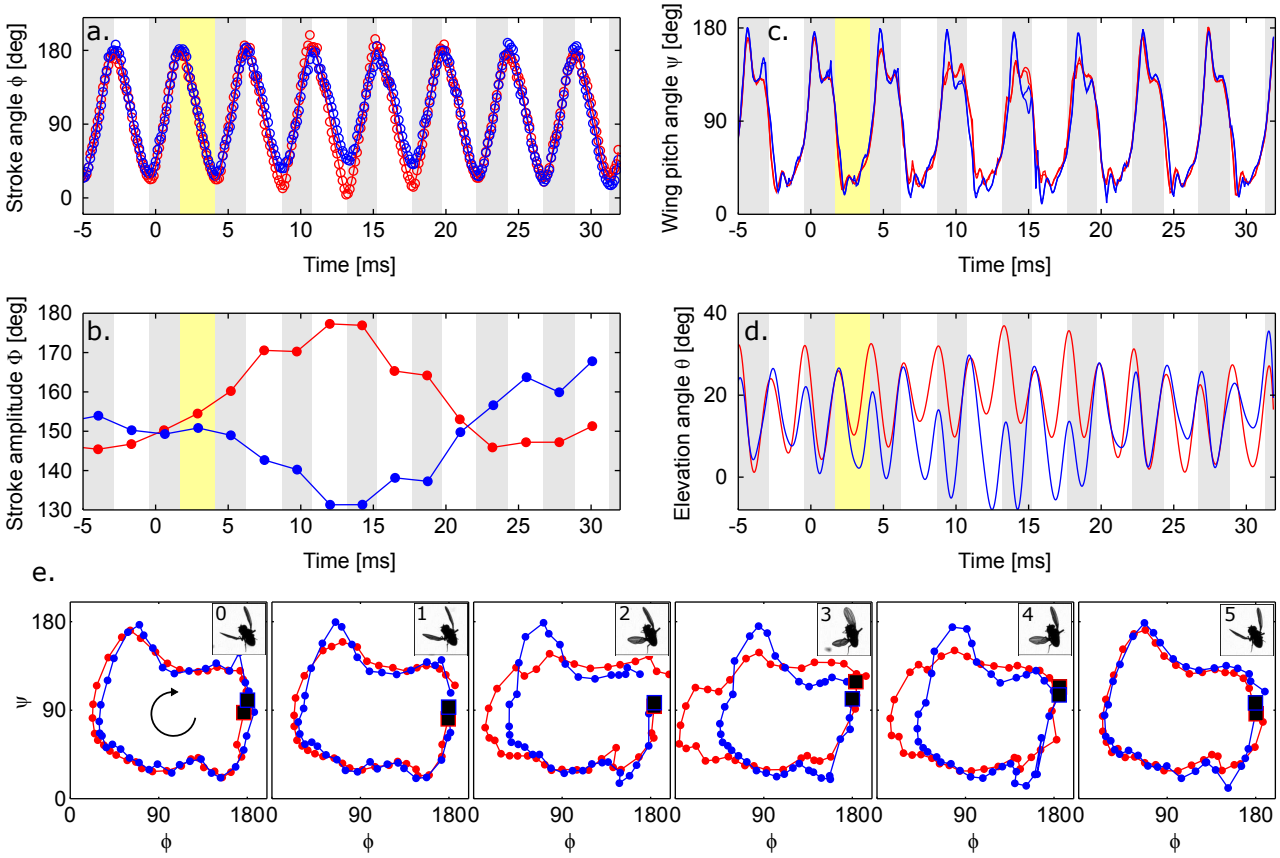

FIG. 2. (Color online) Wing kinematics. (a) The stroke angle ϕ for both wings as a function of time in ms. Throughout the entire figure, red (light gray) indicates the right wing and blue (dark gray) indicates the left wing data The magnetic pulse perturbation is indicated by a yellow strip between t=0 – 5ms. White and gray stripes indicate forward and back stroke, respectively. (b) The peak-to-peak amplitude of the stroke angle Φ for each half-stroke. (c) The wing pitch angles ψ. (d) Wing elevation angles θ. (e) The wing pitch angle ψ as a function of the stroke angle ϕ for both wings, plotted separately for six wing-beats during the roll correction maneuvers. The data in each plot starts when the wings are at their back most position (black squares with red/blue (light/dark gray) outline), and time propagates clockwise as shown by the curved arrow on the left-most plot. Inset images show top-view snapshots of the fly taken when the wings are in their forward-most position (minimum ϕ) during each wing-beat. The wing-beat numbering is the same as in Fig. 1.

obtain their local minimum at the forward-most position of each wing-beat, same as in Fig. 1d.

The first wing-beat in Fig. 2e (labeled 0) started before the onset of the perturbation pulse and represents a typical motion in the (ϕ, ψ) plane. Both wings flapped symmetrically, starting at the back with $\phi \approx 180°$ and $\psi \approx 90°$, then ψ rotated rapidly forward as the wings started their forward stroke. During the forward stroke, which corresponds to the bottom part of the loop, ϕ decreased for both wings while ψ was maintained at $\approx 30°$, resulting in an angle-of-attack of similar value. As the wings approached their forward-most position, namely the local minimum of ϕ around 25°, the wings rotated backwards about their leading edge increasing ψ to 90°. When the wings started to move backwards (ϕ increasing, top part of loop) they also rotated rapidly in pitch, further increasing ψ almost to 180°, where the wing surfaces are almost horizontal. As the back-stroke continued, ψ decreased to $\approx 130°$, corresponding to an angle-of-attack of 50° flapping backwards. This overshoot of the wing towards $\psi \approx 180°$ that looks like a "hump" in the $\psi(\phi)$ curve is highly reproducible in non-maneuvering flight of *D. melanogaster*. At the end of the back-stroke, ψ started a rapid decrease back to 90° as part of the back-flip of the wing before the next stroke.

As the correction maneuver progressed, the top and bottom limits of ϕ values on the $\psi(\phi)$ plots show the increase of the right wing stroke amplitude and the decrease of the left wing stroke amplitude, as in Fig. 2b. Remarkably, along with the ϕ asymmetry, we observe a strong asymmetry in the pitch angle ψ between the two wings: while the left wing kept the characteristic non-maneuvering shape, the "hump" structure of the right wing almost disappeared. This effect increased gradually with the increase of stroke amplitude (wing-beats 1 – 3) and correspondingly decreased until the end of the maneuver, where both wings flapped symmetrically again (wing-beats 4 – 5).

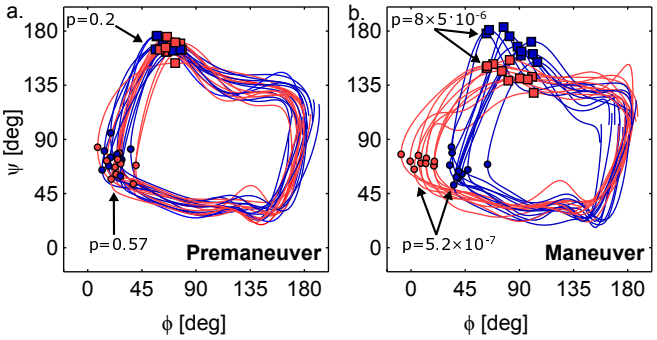

FIG. 3. (Color online) Lissajous-Bowditch plots of ψ as a function of ϕ (a) before and (b) during each of the 10 measured correction maneuvers. Each loop on the (ϕ, ψ) plane corresponds to one wing-beat cycle of one wing. Red (light gray) curves correspond the the "bottom" wing in each maneuver, which is the wing that increases its stroke amplitude. Blue (dark gray) curves correspond to the "top" wing, which reduces its stroke amplitude. A square symbol on each curve indicates the point of maximum ψ in the front half stroke. A circle on each curve indicates the point of minimum (foremost) ϕ. (a) Before the maneuver the curves for the "top" and "bottom" wings are indistinguishable (p-values indicated on the plot). (b) During the maneuver the maximum ψ for the "top" wing is $169° \pm 10°$ (mean±standard deviation) and its value for the "bottom" wing is $144° \pm 8°$ (p-value of 8.5×10^{-6}). The front-most ϕ values during the maneuver are $40° \pm 9°$ for the "top" wing and $9° \pm 9°$ for the "bottom" wing, corresponding to an increase of the stroke amplitude (p-value of 5.2×10^{-7}).

These changes in ψ are consistent throughout our data set, as shown in Fig. 3, which plots the $\psi(\phi)$ curves before the maneuver and during the third wing-beat of each maneuver, when the fly exerts maximum corrective torque. To quantify the differences between the curves we identify two points on each curve: maximum ψ in the front half stroke (squares) and minimum ϕ (circles), corresponding to the front most stroke angle. The "bottom" wing in each maneuver, which increases its stroke amplitude, is shown in red and the "top" wing is shown in blue. Before the onset of the correction maneuver the curves for the "top" and "bottom" wings are indistinguishable. During the maneuver, however, the curves for the "top" and "bottom" wings are significantly different. The maximum ψ for the "top" wing is $169° \pm 10°$ (mean±standard deviation) and its value for the "bottom" wing is $144° \pm 8°$ (p-value of 8.5×10^{-6}). The front-most ϕ values during the maneuver are $40° \pm 9°$ for the "top" wing, corresponding to a decrease of the stroke amplitude, and $9° \pm 9°$ for the "bottom" wing, corresponding to an increase of the stroke amplitude (p-value of 5.2×10^{-7}) [21]. These marked changes in ψ raise two interesting questions. First, do these changes substantially alter the corrective aerodynamic torques? Second, is the fly actively controlling the pitch angle, or is ψ being passively determined by the aerodynamic flows?

B. Wing-pitch modulations contribute to roll corrective torque

To quantify the effect of the ψ asymmetry on the roll correction maneuver, we calculated the total aerodynamic torque exerted by both wings during the wing-beat with the largest ϕ and ψ asymmetry – wing-beat 3 in Figs. 1d and 2e. This wing-beat also generated the peak roll corrective acceleration (Fig. 1d, t=13ms) and, hence, maximum corrective torque. To calculate aerodynamic forces from the measured body and wing kinematics, we used a quasi-steady-state aerodynamic model that was calibrated for fruit-fly wing shape and kinematics using a scaled-up mechanical model [14]. Aerodynamic forces were calculated using the wing orientation and velocity as measured in the lab frame of reference. The wing-tip velocity included the wing velocity with respect to the fly center-of-mass, the fly center-of-mass velocity with respect to the lab, and the fly's body angular velocity with respect to the lab. We verified that the calculated torques are similar for other quasi-steady-state force models [38, 59, 76] as well. The torques were calculated by assuming the aerodynamic force acts at the pressure center of each wing, located at 70% of the wing span from the wing base, and taking the torque arm with respect to the body center of mass. The components of the torque along the three body axes are shown in Fig. 4 for two cases: in the first we used the full wing and body kinematics of wing-beat no. 3 (Fig. 4, black lines) and in the second we used the same kinematics except $\psi(t)$ that was taken from the non-maneuvering wing-beat no. 0 (dashed red lines).

Although changing $\psi(t)$ from the maneuvering to the non-maneuvering kinematics had an effect on the aerodynamic torques, tracing the corresponding changes in the body roll dynamics requires solving the Euler equation of motion for the body. Namely, since 3D rotations do not commute and since the body has nonzero angular velocity, the effects of the plotted torques on roll is non-intuitive. For example, it has been shown that a torque along the body z-axis plays an important part in roll correction and that flies apply torque along this axis particularly during the back-strokes of these maneuvers [21]. Numerical integration of the Euler equations of motion for the two cases in Fig. 4 shows that while the maneuvering wing stroke reduced roll velocity by $\sim3600°s^{-1}$, the same kinematics with the non-maneuvering ψ reduced roll velocity by $\sim2350°s^{-1}$ corresponding to a 35% loss in corrective roll braking. This change is attributed to differences in the torque along the body x or roll axis (Fig. 5a), in the beginning of the wing stroke, as well as to the larger differences in the torque component along the body z axis (Fig. 5c) seen after the middle of the wing-beat, where the "hump" structure is observed. In addition, the mixed kinematics have larger peaks for the torque along the body y axis (Fig. 5b), which roughly corresponds to larger oscillations in body pitch. Performing a similar analysis on all 10 movies in our data

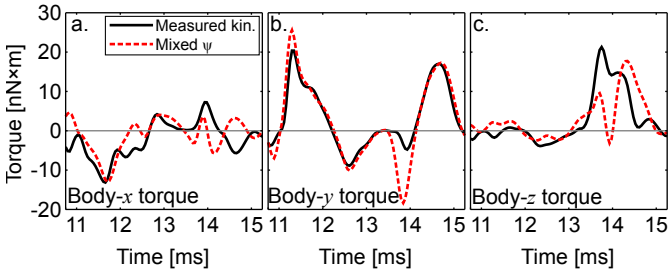

FIG. 4. (Color online) The three components of the aerodynamic torque generated by the two wings during wingbeat no. 3 of the roll maneuver plotted as a function of time in ms (solid black lines). (a-c) The torque components shown are along the (x, y, z) axes of the body frame of reference (defined in Fig. 1b) . The torques were calculated based on the full wing and body kinematics and using a quasi-steady-state aerodynamic force model. Plotted in dashed red (light gray) lines are the aerodynamic torque generated by the same wingbeat kinematics but with $\psi(t)$ taken from a non-maneuvering wing-beat (no. 0). Solving the Euler equation of motion for the body using the torque calculated for these two cases and the experimental initial conditions showed that the measured kinematics reduced the body roll velocity from $2710^\circ s^{-1}$ to $-870^\circ s^{-1}$ (a slowdown of $3580^\circ s^{-1}$), while the "mixed" kinematics reduces the body roll velocity to $360^\circ s^{-1}$ (a slowdown of $2350^\circ s^{-1}$)

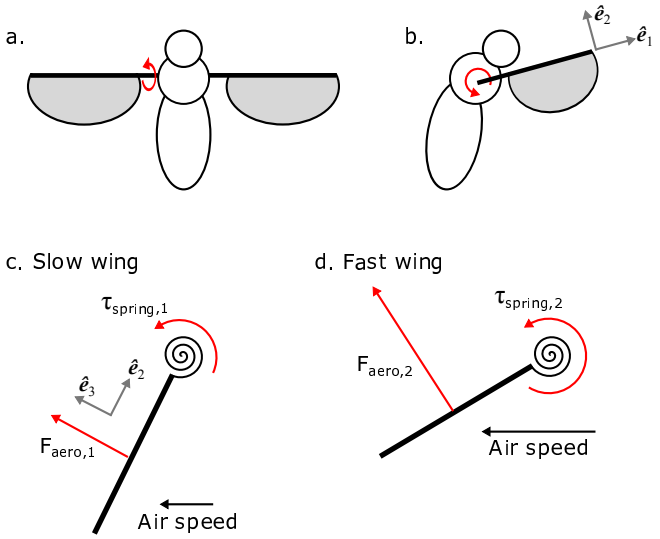

FIG. 5. (Color online) Torsional spring model for wing-pitch. (a, b) A fly scheme with the spring torque indicated by red arrows. The wing frame of reference is shown in (b). (c, d) The operation of the spring (black spiral) on a moving wing (thick black line). For wing with low air speed (c) Red (light gray) line indicates the aerodynamic force that twists the torsional spring such that in steady state (when $\dot{\psi}$=0) the spring torque and aerodynamic torques are balanced. (d) When the wing is moving faster, the aerodynamic force is stronger and so is the torque it generates about the wing base. In steady state the torsional spring is twisted further than in (c) such that the two torques balance at a shallower wing pitch angle.

set showed that changing ψ to the non-maneuvering kinematics resulted in 13% to 65% loss in corrective roll braking, with an average of 37%±17% (mean±standard deviation). These marked differences highlight the importance of the modulations in wing pitch angle imposed by the fly during roll correction.

C. An equation of motion for wing-pitch based on a torsional spring model and quasi-steady aerodynamics

To investigate whether ψ is actively controlled or passively determined by coupling to the flow, we model the wing-hinge as a torsional spring along the wing-pitch axis as shown in Fig. 5 [73]. The torque τ_s generated by the spring is given by:

$$\tau_s(t) = -k\big(\psi(t) - \psi_0\big) - c\dot{\psi}(t), \qquad (1)$$

where k is an elastic coefficient, ψ_0 is the rest angle of the spring, and c is a damping coefficient. The wing is assumed to be a rigid plate, which is a good approximation for *D. melanogaster* wings [14, 55]. The effect of the coupling between the elastic coefficient k and aerodynamic forces on the pitch angle in steady state ($\dot{\psi}$=0) is illustrated in Fig. 5c,d. For simplicity, we consider a wing hinge with a rest angle ψ_0=90° corresponding to a wing with a vertical orientation.

When the wing is moving (Fig. 5c), its airspeed exerts an aerodynamic force that is approximately perpendicular to the wing surface [14]. The aerodynamic force exerts a torque about the wing hinge, rotating the wing such that the spring exerts an opposite torque. In steady state, the pitch angle is deflected from its rest value such that the two torques balance each other. The gravitational torque on the wing is negligible compared with the aerodynamic toque, since the wing weighs ∼0.3% of the fly's weight, while the aerodynamic force is comparable to the fly's weight. When the wing's airspeed is increased as in Fig. 5d, the aerodynamic and spring torques are larger resulting in a greater steady-state pitch deflection with respect to the vertical.

Modulating the wing-pitch rest angle ψ_0 induces an asymmetric change in the angle of attack between the front and back half-strokes, which has been associated with body-yaw maneuvers [73]. The effect of the spring damping coefficient on ψ kinematics is manifested by a counter-torque $-c\dot{\psi}$ proportional to the wing-pitch velocity that damps its motion. Hence, the effect of this damping torque is expected to be most prominent when $\dot{\psi}$ is large, namely when the wing is flipping either at the front or at the back of the wing stroke. Conversely, during the middle parts of each half stroke, when the wing is not rotating much along its pitch axis, the effect of damping is expected to be small.

We derive an equation of motion for the pitch angle ψ

of a single wing described as a thin elliptical plate with typical fruit-fly paramters: major axis equal to the wing span R=2.1mm, minor axis equal to the chord length a=0.7mm, thickness b=$a/50$, and mass m=0.03mg. We work in the wing frame of reference $(\hat{\mathbf{e}}_1, \hat{\mathbf{e}}_2, \hat{\mathbf{e}}_3)$ as defined in Fig. 5, such that the pitch rotation axis is $\hat{\mathbf{e}}_1$. The wing moment of inertia tensor with respect to rotation about the wing-hinge and assuming a thin wing ($b \ll a, R$) is:

$$\mathbf{I} = \begin{pmatrix} I_{11} & I_{12} & 0 \\ I_{21} & I_{22} & 0 \\ 0 & 0 & I_{33} \end{pmatrix} = \frac{3m}{10} \begin{pmatrix} a^2 & \frac{5}{6}aR & 0 \\ \frac{5}{6}aR & R^2 & 0 \\ 0 & 0 & a^2{+}R^2 \end{pmatrix} \tag{2}$$

The off-diagonal terms arise from considering rotations about the wing hinge, which is offset with respect to the wing center of mass.

Due to the flapping motion, the wing frame of reference rotates with respect to the body frame of reference. In addition, the body itself generally rotates in the lab frame of reference during the roll correction maneuver, which generates fictitious torques in the wing frame of reference. The two coordinate transformations from the lab to the body frame and from the body to the wing frame must, therefore, be considered in deriving the equation of motion for ψ. We define $\mathbf{\Omega}$ to be the wing angular velocity vector in the wing frame of reference, such that $\mathbf{\Omega}$ includes both the body and wing angular velocities (see Appendix A). The equation of motion is a balance of angular momentum $\mathbf{L}$=$\mathbf{I\Omega}$ in a rotating frame of reference:

$$\left(\frac{d\mathbf{L}}{dt}\right)_{\text{lab}} = \left(\frac{d\mathbf{L}}{dt}\right)_{\text{wing}} + \mathbf{\Omega} \times \mathbf{L} = \tau_{\text{total}}, \tag{3}$$

in which the total torque is the sum of aerodynamic and spring torques:

$$\tau_{\text{total}} = \tau_{\text{aero}} + \tau_{\text{s}}. \tag{4}$$

The aerodynamic torque τ_{aero} is calculated from the wing and body kinematics as described above, the spring torque τ_{s} is given by Eq. 1. Substituting $\mathbf{L}$=$\mathbf{I\Omega}$ into Eq. 3 and using the thin wing approximation so that I_{33}=I_{11}+I_{22} we find:

$$I_{11}\big(\dot{\Omega}_1 + \Omega_2\Omega_3\big) + I_{12}\big(\dot{\Omega}_2 - \Omega_1\Omega_3\big) = \tau_{\text{total},1} \tag{5}$$

similar to [59], although here both wing and body frames of references are rotating. Hence, to obtain an equation of motion for ψ, we need to obtain an explicit expression for $\ddot{\psi}$. The only place where $\ddot{\psi}$ appears is in $\dot{\mathbf{\Omega}}_1$. We express $\mathbf{\Omega}$ as a sum of the wing angular velocity in the wing frame $\omega_{\text{w,w}}$ and the body angular velocity in the wing frame $\omega_{\text{b,w}}$, namely: $\mathbf{\Omega}$=$\omega_{\text{w,w}}$+$\omega_{\text{b,w}}$, with the wing and body parts given by [77]:

$$\omega_{\text{w,w}} = \begin{pmatrix} \dot{\psi} + \dot{\phi}\sin\theta \\ \dot{\phi}\cos\theta\sin\psi - \dot{\theta}\cos\psi \\ \dot{\phi}\cos\theta\cos\psi + \dot{\theta}\sin\psi \end{pmatrix}. \tag{6}$$

$$\omega_{\text{b,b}} = \begin{pmatrix} \dot{\rho} + \dot{\phi_{\text{b}}}\sin\theta \\ \dot{\phi_{\text{b}}}\cos\theta_{\text{b}}\sin\rho - \dot{\theta_{\text{b}}}\cos\rho \\ \dot{\phi_{\text{b}}}\cos\theta_{\text{b}}\cos\rho + \dot{\theta_{\text{b}}}\sin\rho \end{pmatrix} \tag{7}$$

$$\omega_{\text{b,w}} = T_{\text{b}\to\text{w}} \cdot \omega_{\text{b,b}} \tag{8}$$

The vector $\omega_{\text{b,b}}$ is the body angular velocity in the body frame of reference and the rotation matrix $T_{\text{b}\to\text{w}}$ describes the transformation between the body and wing frames of references (see Appendix A). Note that since θ and θ_{b} are defined with an opposite sign with respect to [77] (see Fig. 1c), their sign in Eqs. 6 and 8 is reversed accordingly. The equation of motion (5) becomes:

$$\begin{aligned} \ddot{\psi} =& \frac{\tau_{\text{total},1}}{I_{11}} - \ddot{\phi}\sin\theta - \dot{\phi}\dot{\theta}\cos\theta - \dot{\omega}_{\text{b,w},1} \\ & - \Omega_2\Omega_3 - \frac{I_{12}}{I_{11}}\Big(\dot{\omega}_{\text{w,w},2} + \dot{\omega}_{\text{b,w},2} - \Omega_1\Omega_3\Big). \end{aligned} \tag{9}$$

The three terms $\dot{\omega}_{\text{b,w},1}$, $\dot{\omega}_{\text{b,w},2}$ and $\dot{\omega}_{2,\text{w},1}$ appear in Appendix A in full form.

Given the torsional spring parameters (k, c, ψ_0), the body orientation $(\phi_{\text{b}}(t), \theta_{\text{b}}(t), \rho(t))$, body center of mass velocity $(\dot{x}(t), \dot{y}(t), \dot{z}(t))$, wing kinematics $(\phi(t), \theta(t))$, and an initial condition for $(\psi, \dot{\psi})$, we solve the equation of motion for $\psi(t)$ using Matlab's ordinary differential equation solver. The body center of mass velocity is used in determining the wing-tip velocity in the lab frame of reference, which is then used to calculate the aerodynamic force. To use experimentally measured data and their time derivatives, we smoothed the data using splines, keeping the smoothing residuals comparable to the measurement accuracy of each kinematic variable.

D. Determining whether wing-pitch modulation is active or passive

We used the above model to find the spring parameters (k, c, ψ_0) that best fit the measured ψ kinematics. For each wing, the fit was performed one wing-beat at a time to find whether the spring parameters accurately describe the wing pitch kinematics and whether the spring parameters change during the correction maneuver. The fitting was achieved by searching the 3D spring parameters space for a triplet (k, c, ψ_0) that minimizes the root-mean-squared error (RMSE) of the calculated ψ with respect to the measured one. The minimization was performed using two methods. In the first method, we scanned a dense 3D grid in parameter space, and for each

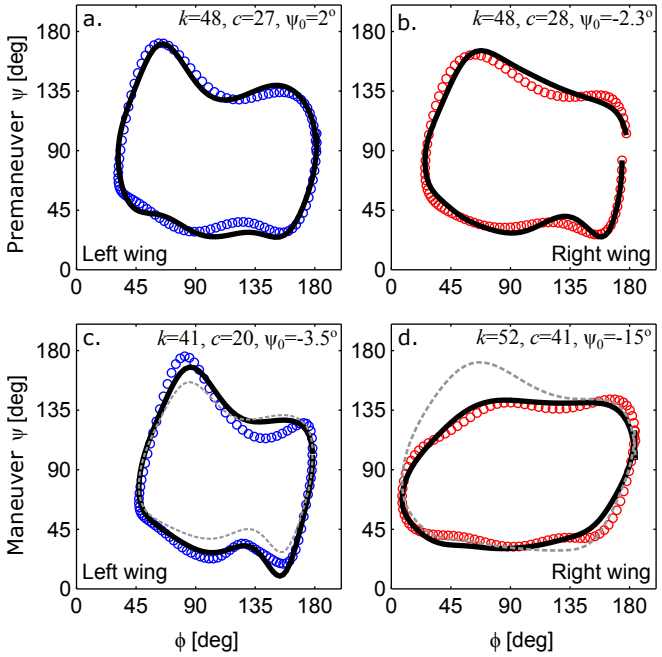

FIG. 6. (Color online) Calculated wing-pitch kinematics from the torsional-spring model plotted in the (ϕ, ψ) plane (solid black lines) along with the smoothed measured kinematics of the left and right wings (circles). Fit results for for a wing-beat before the correction maneuver (no. 0) are shown in (a) for the left wing and in (b) for the right wing. Similarly, fit results for a a maneuvering wing-beat (no. 3) are plotted in (c) for the left wing and in (d) for the right wing. Each plot (a-d) includes also the values of the fitted spring parameters. The mean RMS error values for the fits in (a-d) were: 5.7°, 5.2°, 6.2° and 6.1°, respectively. The torsional spring model captures the salient features of the measured ψ kinematics. The dashed gray curves in (c) and (d) correspond the the calculated ψ kinematics resulting from the wing and body kinematics of the maneuvering wing-beat combined with the fitted spring for the non-maneuvering wing-beat in (a) and (b), respectively.

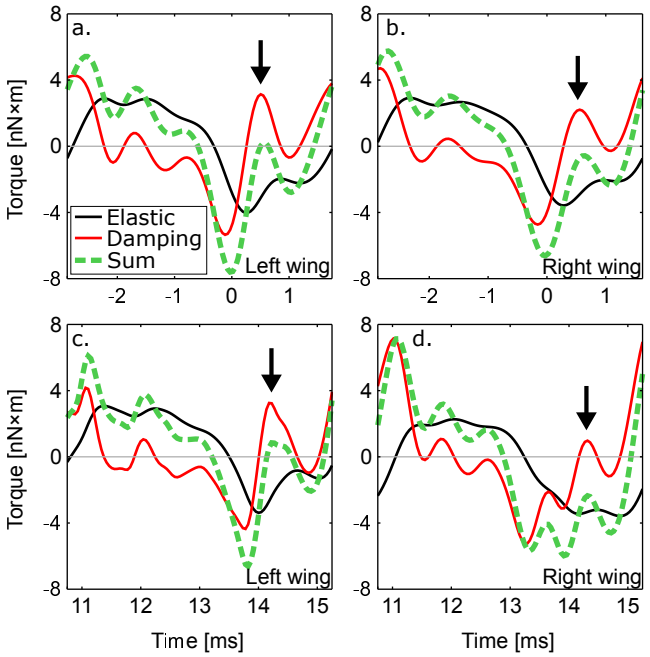

FIG. 7. (Color online) The calculated torque exerted by the spring during the same wing-beats shown in Fig. 6. The torques were calculated using Eq.1 with the fitted spring parameters and the measured wing kinematics. The total spring torque τ_s is plotted in dashed thick green (light gray) lines, the elastic torque term $-k(\psi(t)-\psi_0)$ is plotted in black, and the damping torque term $-c\dot{\psi}$ is plotted in red (darker gray). The wing-beats shown are a non-maneuvering wing-beat for the left (a) and right (b) wing, as well as a manuevering wing-beat for the left (c) and right (d) wing. Black arrows indicate a time when the torque in (d) is more negative than in (a-c) as a result of the damping term after the front wing-flip.

point solved the differential equation for ψ and calculated its RMSE. We then verified that the error landscape is smooth with a single global minimum and picked the spring parameters corresponding to the minimum error. In the second method, we used Matlab's nonlinear trust-region-reflective least-squares optimization algorithm to find the minimum, such that each step of the algorithm entailed solving the differential equation for ψ. Both methods gave quantitatively equivalent results that were within the experimentally determined uncertainty for ψ.

For each fitted spring we estimated the fit confidence intervals (CI) for each of the three fitted parameters. For example, to estimate the CI for k we calculated $\psi(t)$ arising from a spring with $(k+\delta k, c, \psi_0)$. We then search for the maximum positive δk such that the calculated ψ kinematics deviate by less than 4° from the measured values during the entire stroke. This threshold corresponds to the uncertainty of our wing-pitch angle measurement. The lower CI for k was calculated similarly by considering a negative δk. The CI values for the other two spring parameters were calculated using the same method.

To illustrate the types of changes that the spring parameters produce in the $\psi(t)$ curves, we show the fit results for $\psi(t)$ for a non-maneuvering wing-beat and a maneuvering one in Fig. 6. The resulting wing-pitch angles are shown in the (ϕ, ψ) plane (solid lines) along with the measured ψ (symbols). We find that the fitted torsional spring model reproduced the salient features for all four measured ψ kinematics with mean fitting error of 5.8°. For example, the model accurately captured the "hump" in the $\psi(\phi)$ curve seen after the front wing-flip in Fig. 6a,b,c as well as the "hump" absence in the right wing stroke during the maneuvering wing-beat shown in Fig. 6d.

As expected, the fitted spring parameters for both wings before the maneuver were very similar and within each other's CI: k=47 pN×m/deg, c=27 fN×m/(deg s^{-1}), and ψ_0=0° ± 2.3°. During the correction we observe changes in all three spring parameters. However, not all these changes were significant. For example, we find that for the right wing, which increased it's stroke am-

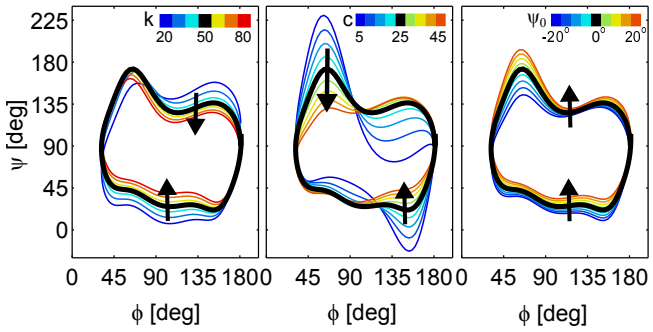

FIG. 8. (Color online) Intuition for the individual effect of each spring parameter on the $\psi(\phi)$ curve. We calculated the wing pitch kinematics of the non-maneuvering wing-beat in Fig. 6a and as a reference used the spring with k=50 pN×m/deg, c=25 fN×m/(deg s^{-1}), and ψ_0=0° (with respect to the vertical). The curves resulting from the reference spring are plotted in solid black lines. (a) Wing pitch curves for increasing k. (b) and (c) show similar curves for increasing c and ψ_0, respectively. Color bars show values of each parameter.

plitude during the roll correction, the elastic coefficient k changed from 48±7.5pN×m/deg to 52.5±6.7pN×m/deg, but that this change fell within the fit CI and was therefore experimentally indistinguishable. In contrast, the rest angle ψ_0 changed from $-2.3° \pm 3.2°$ to $-15° \pm 3.9°$, which fell outside the fit CI and was therefore a detectable change. The most prominent change we observed in this particular maneuver was a 46% increase of the spring *damping* coefficient of the right wing form 28.4± fN×m/(deg s^{-1}) to 41.5±2.6fN×m/(deg s^{-1}) (fitted value ± CI).

To highlight the effect of the different fitted springs on the kinematics of ψ, we solved for $\psi(t)$ of the maneuvering wing-beat but with the spring fitted for the non-maneuvering wing-beat. The resulting $\psi(t)$ is plotted in Fig. 6d in dashed gray, showing a large overshoot of the wing-pitch angle after the front-flip, reminiscent of the non-maneuvering kinematics.

The individual contributions of the elastic and damping torques to the total spring torque during two wing-beats in Fig. 6 are shown in Fig. 7. First, we find that the magnitudes of elastic and damping torques are comparable, indicating that both of them are important in determining wing-pitch kinematics. Second, we find that the spring torques during the maneuvering wing-beat of the right wing (Fig. 7d) are different than the torques during the other wing-beats in Fig. 7a-c. Namely, the torques in Fig. 7d show stronger positive damping torque during the back wing-flips, as well as stronger negative damping torque after the forward flip, where the "hump" appears during non-maneuvering wing-beats.

To gain intuition for the effect that each of the spring parameters induces on wing-pitch, we calculated the $\psi(t)$ kinematics that arise from individually modulating each one of the spring parameters (Fig. 8a). We used the wing and body kinematics of the non-maneuvering wing-beat in Fig. 6 and and considered a reference spring with k=50pN×m/deg, c=25fN×m/(deg s^{-1}), and ψ_0=0° (with respect to the vertical), which is within the CI of the best fitted spring. Increasing k from 20 to 80 pN×m/deg (Fig. 8a) shows that both the top and bottom branches of the $\psi(\phi)$ loops approach the ψ=90° center line (black arrows in Fig. 8) . Increasing k stiffens the spring, such that the aerodynamic force induces smaller ψ deviations from the vertical (ψ=90°). This effect is nonlinear, since the aerodynamic force depends on ψ through the angle of attack. Increasing the damping coefficient c from the reference value of 25 (thick black curve) to 45 fN×m/(deg s^{-1}) (red curve) resulted in the disappearance of the "hump" structure after the front flip (top left part of the curve). In addition, this increase also smoothed a similar smaller feature of the $\psi(\phi)$ curve seen after the back flip (bottom right part of the curve). Conversely, decreasing c from 25 to 5 fN×m/(deg s^{-1}) generated two large "hump" structure after the forward and back wing flips. The most prominent effect of the damping coefficient appears around the wing flips, since these stages of the wing stroke have the largest pitch velocity, which maximizes the damping torque $-c\dot{\phi}$. Increasing the rest angle ψ_0 from −20° to 20° consistently moved both parts of the $\psi(\phi)$ loop towards more positive ψ values (Fig. 8, black arrows). In addition, we find that increasing ψ_0 affected the "hump" structure (top left part of curve), since off-setting the spring make it easier for the aerodyanmic force to bend the wing backwards after the front flip. Taken together, the results in Figs. 6-8 highlight the effect of the spring modulation on the wing-pitch kinematics during roll correction.

We performed the spring fitting procedure described above for all 9 wing-beats of the same maneuver. Figs. 9a-c show the fitted spring parameters as a function of time in wing-beats, such that $t = 0$ corresponds to the wing-beat during which the fly was perturbed. While the changes in the fitted k and ψ_0 values during the maneuver are comparable to the fit CI, the changes in c are much larger than the CI. Fig. 9 shows a significant change in c during the active part of the maneuver. The damping coefficient of the right wing showed an increase of c followed by a decrease to its premaneuver value. The maximum change in c was a 67% increase observed during wing-beat no. 2. Concomitantly, c of the left wing decreased by 32% before increasing back to its value prior to the perturbation. At the end of the maneuver c of the left wing was slightly larger than c of the right wing, corresponding to the roll counter-torque the fly generates at that time. The variations in spring parameters shown in Fig. 9 should be compared against the variations during non-maneuvering flight (Appendix B), which are much smaller: we find standard deviations of ±2.3 pN×m/deg in k, ±2 fN×m/(deg s^{-1}) in c and ±3.5° in ψ_0. We note that the variations in k and c during volitional yaw tuning maneuvers, in which ψ_0 is modulated [73], are also smaller than the modulation of

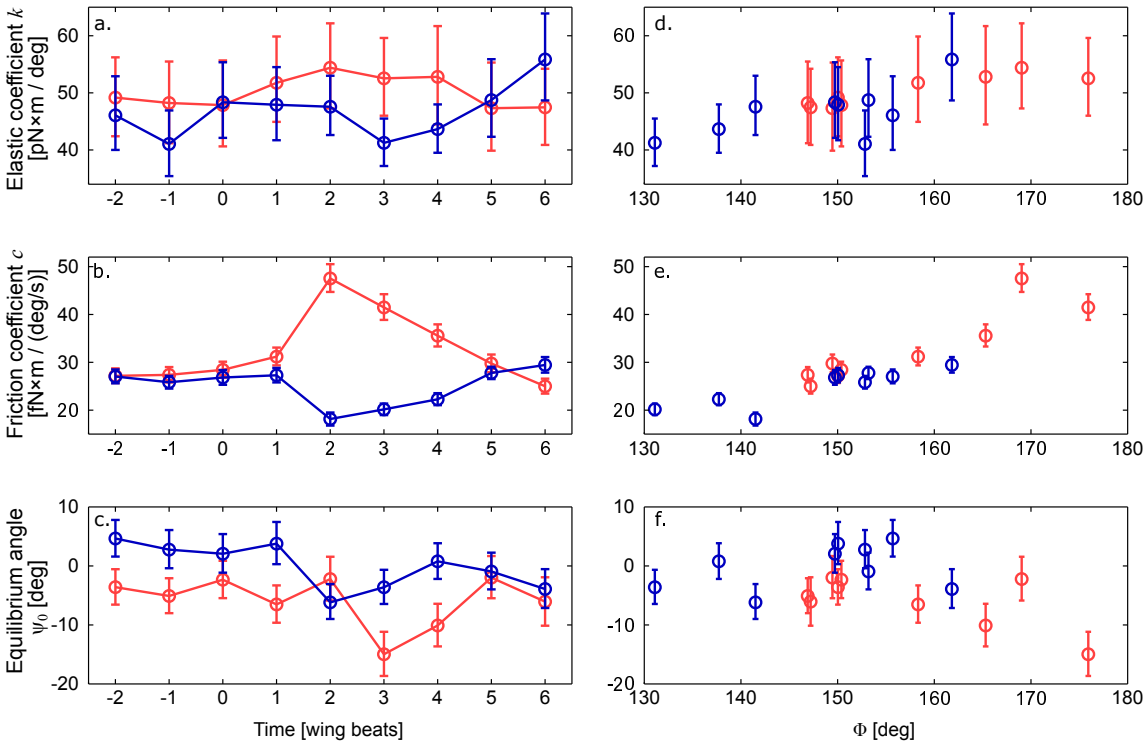

FIG. 9. (Color online) (a-c) the fitted spring parameters k, c, and ψ_0, as a function of time in wing-beats for the maneuver analyzed in Figs. 1-4 and 6. The time t=0 corresponds to wing-beat in which the fly was perturbed. Data is shown for the right wing in red (light gray) and for the left wing in blue (dark gray). Error bars correspond to the fit's confidence intervals (CI). (d-f) The same fit results for k, c, and ψ_0, plotted as a function of the wing-stroke amplitude for the corresponding wing-beat of each wing. The CI are the same as in (a-c).

these parameters reported here.

To further illustrate the the coupling between the wing-stroke and wing-pitch kinematics, we plot the fitted spring parameters as a function the wing-stroke amplitude Φ in each wing-beat of the same maneuver (Figs. 9d-f. The elastic coefficient k shows a slight increase with Φ. The fitted values of ψ_0 are uncorrelated with Φ. In contrast, c shows a clear increase with Φ, indicating that an increasing wing amplitude is correlated with an increasing damping coefficient.

We analyze 10 maneuvers in our data-set and fit the spring coefficients for each wing-beat. The mean pre-perturbation spring parameters are k=46±7 pN×m/deg, c=29±3 fN×m/(deg s^{-1}), and ψ_0= − 7±5° (mean±standard deviation for n = 20). To highlight the changes in the spring parameters during the maneuvers we plot the differences Δk, Δc, and $\Delta\psi_0$ with respect to their values prior to the maneuver (Fig. 10). Figs. 10a-c show the values of these differences for each wing-stroke with separated symbols for the "bottom" wing in the roll maneuver (the wing that flaps with larger Φ, red circles) and the "top" wing (blue squares). While the data for $\Delta\psi_0$ are not correlated with Φ, the data for Δk and Δc are correlated with Φ. Both parameters have correlation coefficients of $\sim$0.5 ± 0.15 (value ± 95% confidence interval) and these correlations are highly significant (p=3.6×10^{-10} for Δk and p=8.8×10^{-8} for Δc). Finally, we note that for Φ values smaller than the mean pre-perturbation value $\Phi_{\rm mean}$=156° ± 2.5° (mean±standard error for n = 20), we see that Δc is scattered around 0 and for $\Phi > \Phi_{\rm mean}$ Δc increases with Φ. To quantify this trend we calculate the means of Δk, Δc, and $\Delta\psi_0$, for the data points with $\Phi \leq \Phi_{\rm mean}$ and similarly for those with $\Phi > \Phi_{\rm mean}$. The means are shown in the bar plots in Figs. 10d-e, with error bars representing the standard error of each mean. This analysis shows that while $\Delta\psi_0$ has no significant Φ dependence (p=0.48), we see a clear Φ dependence of Δk and Δc, with p-values of p=3.6×10^{-10} and p=8.8×10^{-8}, respectively. Together, Fig. 10 shows that both k and c increase at higher wing-stroke amplitude associated with the wing-stroke amplitude asymmetry the flies apply during roll correction maneuvers.

IV. SUMMARY AND OUTLOOK

We used measured body and wing kinematic data of fruit flies to show how asymmetric changes in the spring parameters give rise to differences in wing-pitch kinematics during roll correction maneuvers. In previous work it was shown that flies can control the rest angle ψ_0 to modu-

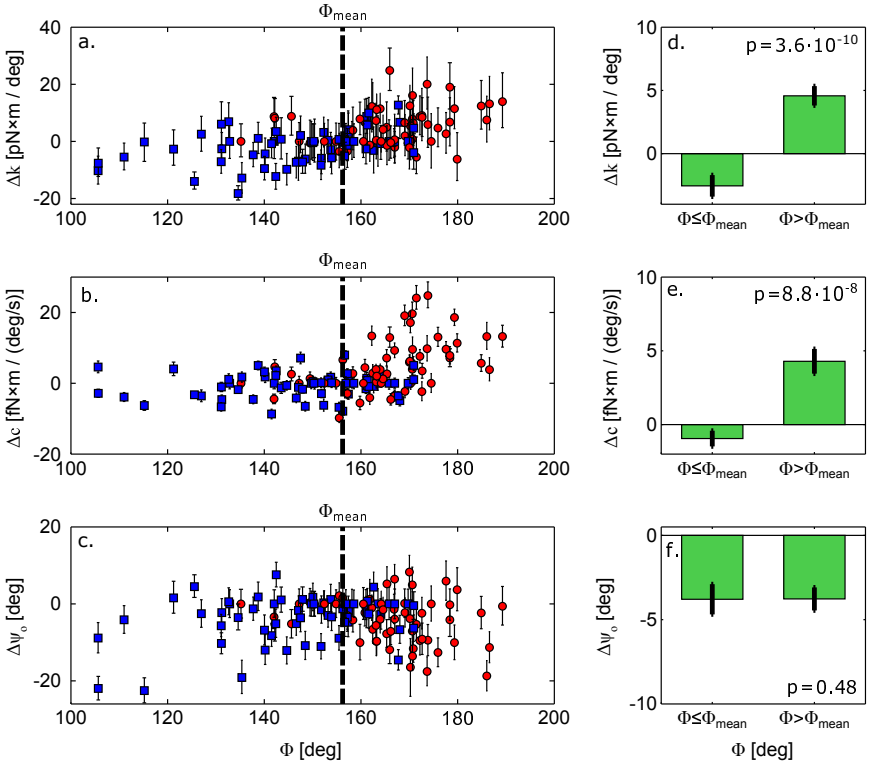

FIG. 10. (Color online) (a-c) The differences in the fitted spring parameters Δk, Δc, and $\Delta\psi_0$ calculated with respect to their values for the corresponding wing prior to each maneuver. The differences are plotted as a function of the wing-stroke amplitude Φ. The first 6 wing-beats for each of the 10 maneuvers analyzed are shown, constituting the active part of each maneuver [21]. Red (light gray) circles indicate data for the "bottom" wing in each roll maneuver, which is the wing that flapped with increased stroke-amplitude to exert roll correcting torque. Blue (dark gray) squares indicate data for the "top" wing in each maneuver. A dashed black line on each plot in (a-c) indicates the mean stroke amplitude before the maneuver Φ_{mean}=156° ± 2.5° (mean±standard error for $n = 20$). Wing-beats with $\Phi > \Phi_{\text{mean}}$. The data for Δk and Δc are correlated with Φ, with correlation coefficients of $\sim 0.5 \pm 0.15$ (value ± 95% confidence interval) and p-values of p=3.6×10^{-10} for Δk and p=8.8×10^{-8} for Δc. (d-f) The mean values of Δk, Δc, and $\Delta\psi_0$, below and above the Φ=165° threshold. Black error bars indicate the standard error of each mean. The p-values in each plot are the results of a t-test comparing the data below and above the threshold.

late their wing pitch and perform yaw turns [73]. Here, we highlight that fruit flies can also modulate the effective spring damping coefficient c and elastic coefficient k. This work builds on previous studies that used a damped torsional spring model [62, 64, 65, 73, 78] and on studies that showed that the torques exerted by the hinge can be approximated by a such a spring by analytically recovering the spring-torque from measured kinematic data [56, 73]. Here, we use this torsional spring model to directly solve the equation of motion for the wing-pitch and reproduce its intricate kinematics.

Our results directly address the question of whether ψ is actively or passively controlled. Together with a previous analysis on yaw turns in flies [73], our findings suggest that flies take advantage of the passive coupling between aerodynamics and the torsional spring to indirectly control their wing-pitch kinematics by modulating the spring parameters: damping coefficient, rest angle and elastic coefficient. Thus, flies can control their wing-pitch kinematics on a sub-wing-beat time-scale by modulating all the effective spring parameters on longer time-scales.

The results presented here raise a few open questions. For example, what physiological mechanism generates the effective behavior of a torsional spring and, more specifically, how damping can be physiologically implemented and modulated. We can propose two alternative mechanisms for damping generation: the first is an active mechanism based on a muscle exerting negative work along the pitch axis, such as the first basalare muscle (b1) that has been proposed to be related to wing-pitch control [4, 79]. The activity pattern of the basalare muscles (b1, b2, and b3) as well as the III2-III3 muscles have been correlated with the position of the ventral (frontmost) flip of the wing stroke angle, making these muscles additional candidates for wing-pitch control [6]. The second proposed mechanism is a passive mechanism that increases torsional damping at large wing stroke amplitudes (see Figs. 9e and 10b,e). Our results cannot discriminate between these two proposed mechanisms. A related open question is the implication of passive aerodynamic effects

to the design of insect wings through their intricate venation patten [80–82]. Future extensions of this work may include more detailed spring models such as an asymmetric linear spring [52] and nonlinear springs [58], as well as studying wing pitch kinematics in insects with flexible wings. Finally, applying the methods developed here to other organism may reveal whether the modulations of relatively simple bio-mechanic parameters that allow an animal to control its complex motion, is a general design principle of biolocomotion.

Appendix A: Equation of motion for ψ

Given below are the terms in the equation of motion for ψ (eq. 9) that were implicitly specified in the main text. The rotation matrix $T_{\mathrm{b}\to\mathrm{w}}$ from the body frame of reference to the wing frame of reference consists of two rotations: a rotation from the body frame to the wing-stroke place frame followed by a rotation from the wing-stroke frame to the wing frame. We define $M(\alpha,\beta,\gamma)$ as the Euler rotation matrix corresponding to a rotation of α radians in yaw, β radians in pitch, and γ radians in roll. The matrix $T_{\mathrm{b}\to\mathrm{w}}$ becomes:

$$T_{\mathrm{b}\to\mathrm{w}} = M(\phi,\theta,\psi)\, M(0,\theta_{b0},0)^T, \tag{A1}$$

where θ_{b0} is the measured pitch angle of the stroke plane with respect to the body frame of reference. For fruit flies we typically measure $\theta_{b0}\approx 45^\circ$. The remaining terms are in eq. 9 are:

$$\begin{aligned}\dot{\omega}_{\mathrm{w,w},2} = &-\ddot{\theta}\cos\psi + \ddot{\phi}\cos\theta\sin\psi + \dot{\theta}\dot{\psi}\sin\psi \\ &-\dot{\phi}\dot{\theta}\sin\theta\sin\psi + \dot{\phi}\dot{\psi}\cos\theta\cos\psi\end{aligned} \tag{A2}$$

$$\dot{\omega}_{\mathrm{b,w}} = \dot{T}_{\mathrm{b}\to\mathrm{w}}\cdot\omega_{\mathrm{b,b}} + T_{\mathrm{b}\to\mathrm{w}}\cdot\dot{\omega}_{\mathrm{b,b}}. \tag{A3}$$

$$\Omega_1\Omega_3 = \left(\omega_{\mathrm{w,w},1}+\omega_{\mathrm{b,w},1}\right)\left(\omega_{\mathrm{w,w},3}+\omega_{\mathrm{b,w},3}\right) \tag{A4}$$

We note that differences between the parameter values determined in [73] and the current manuscript are primarily due to the more accurate equation of motion used in the present study. The equation of motion used here considers the wing rotating frame of reference that results in fictitious torques along the wing pitch axis.

Appendix B: Spring parameters during non-maneuvering flight

To test whether the spring parameters change when a fly is not maneuvering, we analyzed a movie of a fly hovering with no magnetic pin glued on its back and, hence, no external perturbation. The movie consisted of 22 wing-beats in which the fly's center-of-mass speed was lower than 60mm s^{-1}, equivalent to 0.09 body-lengths per wing-beat. The mean stroke amplitude of both wings was 151.4±2° (mean±standard deviation, n=44). The fitted spring parameters for every wing-beat of each wing are plotted in Figure 11. The mean and standard deviation in the fitted spring parameters for the left wing are k=47±2.6 pN×m/deg, c=29±1.6 fN×m/(deg s^{-1}), and ψ_0= − 10±3.5°. The values for the right wing are k=54±2.3 pN×m/deg, c=24±2 fN×m/(deg s^{-1}), and ψ_0= − 4±3.5°. The variation in k and c is markedly smaller than the variation of these parameters during roll correction maneuvers.

ACKNOWLEDGMENTS

We would like to thank Oded Gottlieb, John Guckenheimer, Sarah Iams, Brian Leahy and Samuel Whitehead for fruitful discussions. T.B. was supported by the Cross Disciplinary Postdoctoral Fellowship of the Human Frontier Science Program. In addition the work was supported in part by an NSF-CBET award number 0933332 and an ARO award number 61651-EG.

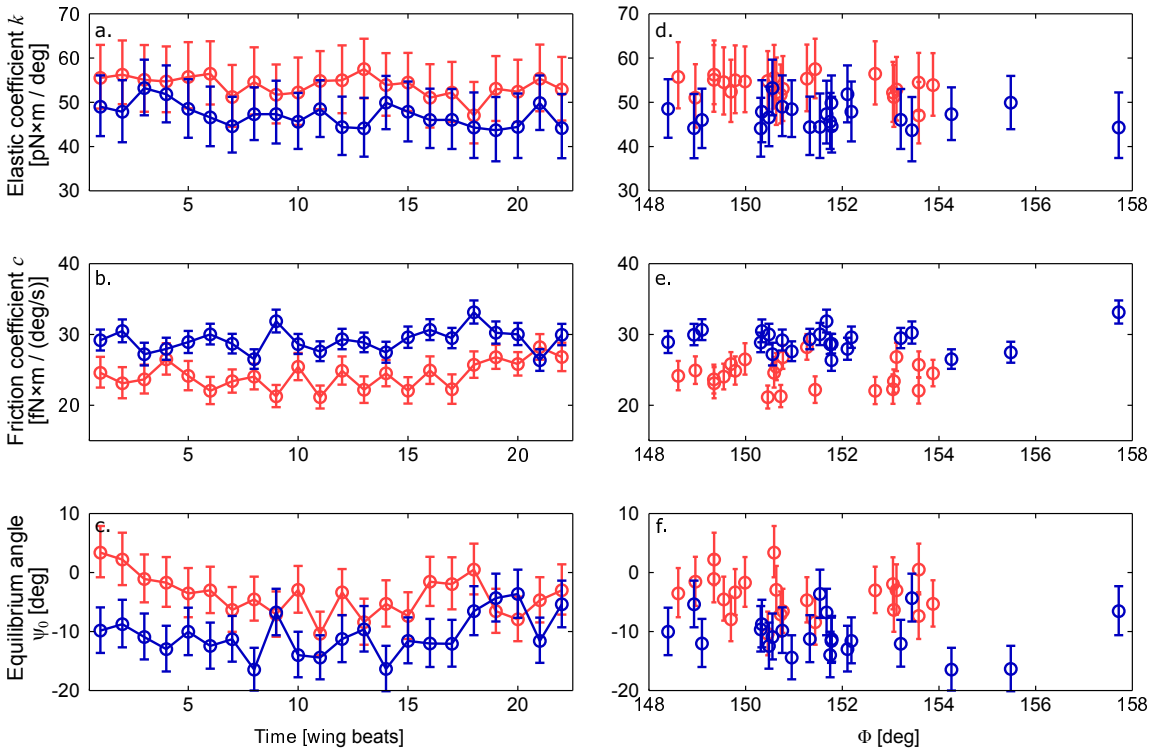

FIG. 11. (Color online) (a-c) the fitted spring parameters k, c, and ψ_0, as a function of time in wing-beats for a fly hovering for 22 wing-beats. Data is shown for the right (red / light gray) and left (blue / dark gray) wing and the error bars correspond to the fit's confidence intervals (CI). The mean and standard deviation values for the spring parameters of the left (L) and right (R) wings are: k_L=47±2.6 pN×m/deg, c_L=29±1.6 fN×m/(deg s^{-1}), $\psi_{0,\mathrm{L}}$=−10±3.5°, k_R=54±2.3 pN×m/deg, c_R=24±2 fN×m/(deg s^{-1}), and $\psi_{0,\mathrm{R}}$= − 4±3.5°. (d-f) The same fit results for k, c, and ψ_0, plotted as a function of the wing-stroke amplitude for the corresponding wing-beat of each wing. The CI are the same as in (a-c). The mean stroke amplitude of both wings was 151.4±2° (mean±standard deviation, n=44)

[1] R. Dudley, *The biomechanics of insect flight: form, function, evolution* (Princeton University Press, 2002).
[2] J. G. Kingsolver and M. Koehl, Annual Review of Entomology **39**, 425 (1994).
[3] G. K. Taylor and H. G. Krapp, Advances in Insect Physiology **34**, 231 (2007).
[4] M. Tu and M. Dickinson, The Journal of Experimental Biology **192**, 207 (1994).
[5] M. Tu and M. Dickinson, Journal of Comparative Physiology A **178**, 813 (1996).
[6] C. N. Balint and M. H. Dickinson, The Journal of Experimental Biology **204**, 4213 (2001).
[7] C. N. Balint and M. H. Dickinson, The Journal of Experimental Biology **207**, 3813 (2004).
[8] M. A. Frye and M. H. Dickinson, Current opinion in neurobiology **14**, 729 (2004).
[9] M. A. Frye, Current opinion in neurobiology **20**, 347 (2010).
[10] J. L. Fox, A. L. Fairhall, and T. L. Daniel, Proceedings of the National Academy of Sciences **107**, 3840 (2010).
[11] T. Weis-Fogh and M. Jensen, Philosophical Transactions of the Royal Society of London.Series B, Biological Sciences , 415 (1956).
[12] T. Weis-Fogh, The Journal of Experimental Biology **59**, 169 (1973).
[13] C. Ellington, Philosophical Transactions of the Royal Society of London.Series B, Biological Sciences , 41 (1984).
[14] M. H. Dickinson, F. O. Lehmann, and S. P. Sane, Science **284**, 1954 (1999).
[15] S. P. Sane, The Journal of Experimental Biology **206**, 4191 (2003).
[16] Z. J. Wang, Annu. Rev. Fluid Mech. **37**, 183 (2005).
[17] M. Sun, Rev. Mod. Phys. **86**, 615 (2014).
[18] M. H. Dickinson, Philosophical Transactions of the Royal Society of London.Series B: Biological Sciences **354**, 903 (1999).
[19] L. Ristroph, A. J. Bergou, G. Ristroph, K. Coumes, G. J. Berman, J. Guckenheimer, Z. J. Wang, and I. Cohen, Proceedings of the National Academy of Sciences **107**, 4820 (2010).
[20] B. Cheng, X. Deng, and T. L. Hedrick, The Journal of Experimental Biology **214**, 4092 (2011).
[21] T. Beatus, J. Guckenheimer, and I. Cohen, Journal of The Royal Society Interface **12** (2015).
[22] S. C. Whitehead, T. Beatus, L. Canale, and I. Cohen, arXiv preprint arXiv:1503.06507 (2015).
[23] J. M. Birch and M. H. Dickinson, The Journal of Experimental Biology **206**, 2257 (2003).
[24] F.-O. Lehmann, The Journal of Experimental Biology **211**, 224 (2008).
[25] L. A. Miller and C. S. Peskin, The Journal of Experimental Biology **212**, 3076 (2009).
[26] W. Shyy, H. Aono, S. K. Chimakurthi, P. Trizila, C.-K. Kang, C. E. Cesnik, and H. Liu, Progress in Aerospace Sciences **46**, 284 (2010).
[27] C.-k. Kang and W. Shyy, Journal of The Royal Society Interface **11**, 20140933 (2014).
[28] H. Masoud and A. Alexeev, Physical Review E **81**, 056304 (2010).
[29] M. J. Shelley and J. Zhang, Annual Review of Fluid Mechanics **43**, 449 (2011).
[30] S. Vogel, Journal of Experimental Botany **40**, 941 (1989).
[31] L. Ristroph, M. N. Moore, S. Childress, M. J. Shelley, and J. Zhang, Proceedings of the National Academy of Sciences **109**, 19606 (2012).
[32] S. Vogel, *Life in moving fluids: the physical biology of flow* (Princeton University Press, 1996).
[33] J. Pringle, *Insect flight* (Cambridge University Press, 1957).
[34] M. H. Dickinson and M. S. Tu, Comparative Biochemistry and Physiology Part A: Physiology **116**, 223 (1997).
[35] A. Wisser and W. Nachtigall, Zoomorphology **104**, 188 (1984).
[36] G. Nalbach, Journal of Comparative Physiology A: Neuroethology, Sensory, Neural, and Behavioral Physiology **165**, 321 (1989).
[37] S. M. Walker, D. A. Schwyn, R. Mokso, M. Wicklein, T. Müller, M. Doube, M. Stampanoni, H. G. Krapp, and G. K. Taylor, PLoS biology **12**, e1001823 (2014).
[38] S. P. Sane and M. H. Dickinson, The Journal of Experimental Biology **205**, 1087 (2002).
[39] S. P. Windsor, R. J. Bomphrey, and G. K. Taylor, Journal of The Royal Society Interface **11**, 20130921 (2014).
[40] H.-T. Lin, I. G. Ros, and A. A. Biewener, Journal of The Royal Society Interface **11**, 20140239 (2014).
[41] E. Roth, K. Zhuang, S. A. Stamper, E. S. Fortune, and N. J. Cowan, The Journal of Experimental Biology **214**, 1170 (2011).
[42] S. Viollet and J. Zeil, The Journal of Experimental Biology **216**, 1280 (2013).
[43] N. Cowan, J. Lee, and R. Full, Journal of Experimental Biology **209**, 1617 (2006).
[44] N. J. Cowan and E. S. Fortune, The Journal of neuroscience **27**, 1123 (2007).
[45] E. Roth, S. Sponberg, and N. Cowan, Current opinion in neurobiology **25**, 54 (2014).
[46] N. J. Cowan, M. M. Ankarali, J. P. Dyhr, M. S. Madhav, E. Roth, S. Sefati, S. Sponberg, S. A. Stamper, E. S. Fortune, and T. L. Daniel, Integrative and comparative biology , icu050 (2014).
[47] J. P. Dyhr, K. A. Morgansen, T. L. Daniel, and N. J. Cowan, The Journal of experimental biology **216**, 1523 (2013).
[48] M. S. Madhav, S. A. Stamper, E. S. Fortune, and N. J. Cowan, The Journal of experimental biology **216**, 4272 (2013).
[49] R. Å. Norberg, Journal of comparative physiology **81**, 9 (1972).
[50] A. R. Ennos, The Journal of Experimental Biology **127**, 355 (1987).
[51] A. R. Ennos, The Journal of Experimental Biology **140**, 161 (1988).
[52] A. R. Ennos, The Journal of Experimental Biology **140**, 137 (1988).
[53] A. R. Ennos, The Journal of Experimental Biology **142**, 87 (1989).
[54] J. A. Miyan and A. W. Ewing, The Journal of Experimental Biology **136**, 229 (1988).
[55] S. A. Combes and T. L. Daniel, The Journal of Experimental Biology **206**, 2999 (2003).
[56] A. J. Bergou, S. Xu, and Z. Wang, Journal of Fluid Mechanics **591**, 321 (2007).

[57] D. Ishihara, Y. Yamashita, T. Horie, S. Yoshida, and T. Niho, The Journal of Experimental Biology **212**, 3882 (2009).

[58] Z. Khan, K. Steelman, and S. Agrawal, in *Robotics and Automation, 2009. ICRA'09. IEEE International Conference on* (IEEE, 2009) pp. 3651–3656.

[59] J. Whitney and R. Wood, Journal of Fluid Mechanics **660**, 197 (2010).

[60] K. Y. Ma, P. Chirarattananon, S. B. Fuller, and R. J. Wood, Science **340**, 603 (2013).

[61] Z. Teoh and R. J. Wood, in *Robotics and Automation (ICRA), 2013 IEEE International Conference on* (IEEE, 2013) pp. 1381–1388.

[62] D.-w. Peng and M. Milano, Journal of Fluid Mechanics **717**, R1 (2013).

[63] D. Ishihara, T. Horie, and T. Niho, Bioinspiration & biomimetics **9**, 046009 (2014).

[64] L. Hines, D. Campolo, and M. Sitti, Robotics, IEEE Transactions on **30**, 220 (2014).

[65] J. Toomey and J. D. Eldredge, Physics of Fluids (1994-present) **20**, 073603 (2008).

[66] M. Vanella, T. Fitzgerald, S. Preidikman, E. Balaras, and B. Balachandran, The Journal of Experimental Biology **212**, 95 (2009).

[67] D. Ishihara, T. Horie, and M. Denda, The Journal of Experimental Biology **212**, 1 (2009).

[68] J. Zhang, N.-S. Liu, and X.-Y. Lu, Journal of Fluid Mechanics **659**, 43 (2010).

[69] H. Mahjoubi and K. Byl, Journal of Intelligent & Robotic Systems **70**, 181 (2013).

[70] C. Chevallereau, M. Porez, and F. Boyer, in *Intelligent Robots and Systems (IROS 2014), 2014 IEEE/RSJ International Conference on* (IEEE, 2014) pp. 3404–3410.

[71] Y. Qin, B. Cheng, and X. Deng, in *Intelligent Robots and Systems (IROS 2014), 2014 IEEE/RSJ International Conference on* (IEEE, 2014) pp. 3193–3200.

[72] Y. Segev, *Lift Generation by Flapping Wings in Hover*, Master's thesis, Technion – Israel Institute of Technology (2014).

[73] A. J. Bergou, L. Ristroph, J. Guckenheimer, I. Cohen, and Z. J. Wang, Physical review letters **104**, 148101 (2010).

[74] J. Young, S. M. Walker, R. J. Bomphrey, G. K. Taylor, and A. L. Thomas, Science **325**, 1549 (2009).

[75] L. Ristroph, G. J. Berman, A. J. Bergou, Z. J. Wang, and I. Cohen, The Journal of Experimental Biology **212**, 1324 (2009).

[76] G. J. Berman and Z. J. Wang, Journal of Fluid Mechanics **582**, 153 (2007).

[77] H. Goldstein, C. Poole, and J. Safko, *Classical mechanics*, 3rd ed. (TBS, 2001).

[78] P. Parks, B. Cheng, Z. Hu, and X. Deng, in *Intelligent Robots and Systems (IROS), 2011 IEEE/RSJ International Conference on* (IEEE, 2011) pp. 574–579.

[79] M. H. Dickinson, F.-O. Lehmann, and K. Götz, The Journal of experimental biology **182**, 173 (1993).

[80] R. J. Wootton, Journal of Zoology **193**, 447 (1981).

[81] R. Wootton, R. Herbert, P. Young, and K. Evans, Philosophical Transactions of the Royal Society of London. Series B: Biological Sciences **358**, 1577 (2003).

[82] S. Combes and T. Daniel, The Journal of Experimental Biology **206**, 2979 (2003).